

# Measurement of in-plane thermal diffusivity of thin film using a regression methodology based on Bayesian optimization algorithm

Cite as: Rev. Sci. Instrum. 96, 084903 (2025); doi: 10.1063/5.0285181

Submitted: 13 June 2025 • Accepted: 18 July 2025 •

Published Online: 7 August 2025



View Online



Export Citation



CrossMark

Maochao Lv,<sup>1,a)</sup> Qinmeng Jiang,<sup>2</sup> Hui Liu,<sup>1</sup> Yanhui Zhang,<sup>2</sup> Jie Yang,<sup>2</sup> and Jianli Wang<sup>2,a)</sup>

## AFFILIATIONS

<sup>1</sup> School of Information and Control Engineering, China University of Mining and Technology, Xuzhou 221008, China

<sup>2</sup> Jiangsu Key Laboratory for Design and Manufacturing of Precision Medicine Equipment, Department of Mechanical Engineering, Southeast University, Nanjing 210096, China

<sup>a)</sup> Authors to whom correspondence should be addressed: [lb20060004@cumt.edu.cn](mailto:lb20060004@cumt.edu.cn) and [wangjianli@seu.edu.cn](mailto:wangjianli@seu.edu.cn)

## ABSTRACT

Lock-in thermography is widely used in determining the thermal properties of films by extracting the amplitude and phase of thermal waves. However, achieving high phase detection accuracy typically requires sophisticated infrared (IR) cameras. In this work, we present a regression methodology based on Bayesian optimization to determine the in-plane thermal diffusivity of thin films. Unlike conventional approaches that rely on lock-in algorithms, where amplitude and phase are treated as intermediate quantities, our method directly incorporates time-sequential thermograms into the regression process. The thermal diffusivity and phase offset are automatically extracted by minimizing the mean absolute error between measured and simulated normalized temperatures. This method is validated through measurements on a stainless-steel film, demonstrating that accurate results can be achieved using only a few thermograms per modulation period. These findings highlight the feasibility, robustness, and reduced system requirements of the proposed approach, making it particularly promising for characterizing composite films and advanced thermal interfacial materials.

Published under an exclusive license by AIP Publishing. <https://doi.org/10.1063/5.0285181>

## I. INTRODUCTION

Understanding the thermophysical properties of thin films is essential for a wide range of applications spanning microelectronics, flexible devices, and advanced composites.<sup>1</sup> Although commercial laser flash analysis is widely used for characterizing the thermophysical characterization of films with millimeter-scale thickness, its reliability degrades for thin films at the micrometer-scale, particularly for in-plane diffusivity measurements.<sup>2</sup>

Lock-in thermography is one of the most widely used non-destructive techniques for determining the thermal properties of thin films,<sup>3–12</sup> detecting subsurface defects,<sup>13–15</sup> and evaluating thermal contact resistances.<sup>16</sup> In this technique, the sample surface is periodically heated by a modulated light source, and the resulting spatial distribution of temperature oscillations is recorded by an Infrared (IR) camera. Lock-in thermography has been utilized to measure a variety of thermal properties under different illumination sources and configurations. Among these, the laser spot

is the most used heat source, enabling the measurement of both isotropic<sup>4–7,11</sup> and anisotropic<sup>6</sup> films from the spatial distribution of amplitude and phase of the surface temperature. A laser line heat source has been particularly employed to measure the thermal diffusivity of anisotropic samples in arbitrary in-plane directions.<sup>8–10</sup> The planar heat source, on the other hand, has been used to characterize through-thickness thermal diffusivity as well as thermal contact resistance<sup>16</sup> by analyzing thermographic images in the frequency domain.

Traditionally, the amplitude and phase of a thermal wave are extracted using offline lock-in analysis, such as Fast Fourier transforms (FFT)<sup>17,18</sup> and the Goertzel algorithm.<sup>19</sup> By solving heat conduction equations, thermal properties can be derived from the temperature amplitude and phase profiles using the slope method. For instance, the in-plane thermal diffusivity can be calculated from the slope of the phase lag vs lateral distance to the heating spot, or from the slope of the natural logarithm of the amplitude vs lateral distance.<sup>4,6,8</sup> In these analyses, the accuracy of phase lag

measurements is critical. To minimize uncertainty in the phase signal, the modulation heating (lock-in frequency) and the sampling events should be synchronized, enabling precise lock-in correlation. In addition, high-quality infrared cameras, featuring high frame rates (exceeding 100 Hz) and low noise equivalent temperature difference (NETD <50 mK), are typically adopted to capture time-sequential thermograms.<sup>3,5–11,13–16</sup> Recently, Ishizaki and Nagano<sup>6</sup> successfully measured the in-plane thermal diffusivity of various films using a non-research-grade thermographic camera with a frame rate of 25 Hz and NETD of 100 mK. The camera operated in free-run mode and lacked integrated lock-in capabilities. The offline FFT method was utilized for phase extraction; however, limitations in phase detection accuracy remained unsolved.

Inspired by machine learning algorithms that autonomously extract underlying features from signals without requiring domain-specific expertise, we developed a regression methodology based on a Bayesian optimization algorithm to determine the in-plane thermal diffusivity of thin films. Unlike conventional approaches that rely on lock-in algorithms and analytical solutions to heat conduction equations, where amplitude and phase are treated as intermediate features, our method eliminates these steps entirely. Instead, a single cycle of time-sequential thermograms, recorded using a free-running, non-research-grade IR camera, was directly fed into the regression process. The in-plane thermal diffusivity of a stainless-steel film was accurately extracted using as few as 7 thermograms per modulation period, thereby validating the feasibility and effectiveness of the proposed methodology.

## II. EXPERIMENTAL AND METHODS

### A. Experimental setup

Figure 1 presents a schematic diagram and a photograph of the experimental setup. A fiber-coupled laser (532 nm wavelength and 1 W normal maximum power) served as the light source. The laser intensity was periodically modulated at a frequency  $f_0$ . After passing

through a beam expander, the modulated laser beam was directed onto the sample back surface using some optical elements, including a 45° mirror and a focusing lens. A beam analyzer (Thorlabs) was used to measure the laser spot radius, which was determined to be about 10.0  $\mu\text{m}$ . An optical attenuator was placed before the beam expander to prevent laser-induced damage by maintaining the laser intensity below the damage threshold of the samples. The laser power was calibrated with a power meter and generally adjusted between 0.05 and 0.3 W for the experiments.

On the detection side, infrared radiation (8–14  $\mu\text{m}$  wavelength) emitted from the front surface of the sample was captured by a long-wave IR camera equipped with a macro lens, providing a spatial resolution of 20.0  $\mu\text{m}/\text{pixel}$ . The camera's field of view was  $\sim 12.8 \times 9.6 \text{ mm}^2$ , corresponding to a resolution of  $640 \times 480$  pixels. After the temperature reached a quasi-steady state, thermal images were recorded as a video in AVI format at a frame rate of 20 Hz. In conventional lock-in thermography, the modulation signal and image acquisition are typically synchronized using a shared trigger. However, as illustrated in Fig. 1(a), the IR camera in this study operated in a free-run mode, so synchronization between the modulation signal and the thermal image acquisition was not required.

### B. Image processing

Figure 2 shows the image processing workflow. The thermographic video was first decomposed into several hundred individual frames. Figure 3 presents four representative IR images. To enhance detection sensitivity, the IR images were processed in grayscale, though color thermograms are displayed in Fig. 3 for visual guidance. Since grayscale images are limited to digital values between 0 and 255, the temperature scale bar varies across frames to ensure measurement accuracy. The upper and lower bounds of each temperature scale were identified using the open-source Tesseract Optical Character Recognition tool.<sup>20</sup> Subsequently, the digital grayscale

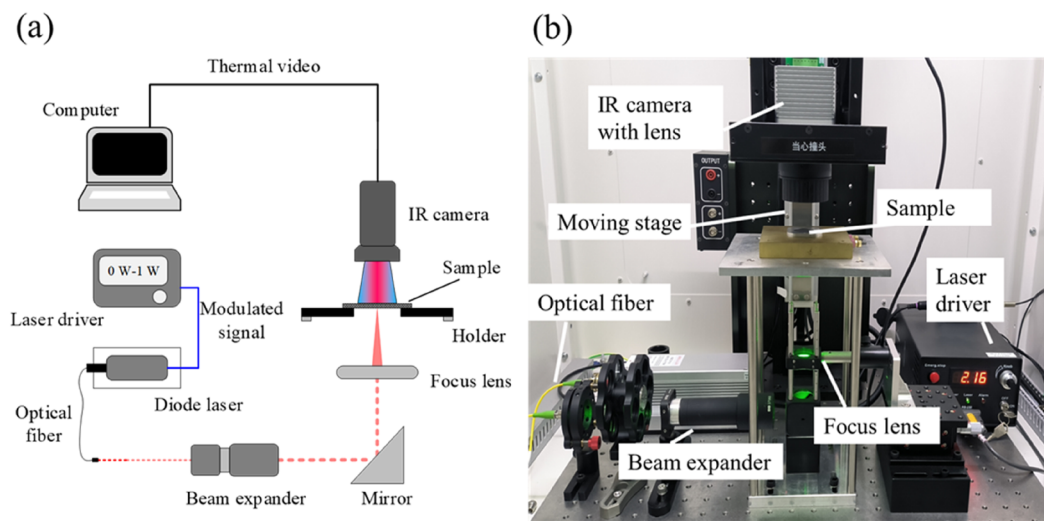
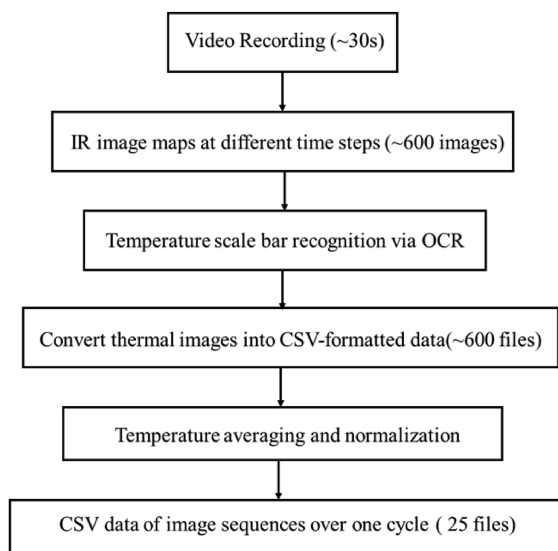


FIG. 1. Experimental apparatus. (a) Schematic diagram and (b) photograph of the configuration.



**FIG. 2.** Flow chart of thermal image processing at a modulation frequency  $f_0 = 0.8$  Hz and an infrared camera frame rate of 20 Hz.

values of each pixel were converted to temperature, and the resulting temperature matrices were saved as two-dimensional CSV files. To reduce data redundancy, the temperatures were temporally compressed into a single modulation period by averaging across multiple cycles. For instance, at a modulation frequency  $f_0 = 0.8$  Hz, a 30-s video consists of 600 thermograms captured at 20 Hz. These frames span 24 full modulation periods, and the data were averaged and compressed into 25 representative CSV files, each corresponding to a time step within one modulation cycle.

The temperature normalization was applied to scale the data within the range of [0, 1], ensuring consistent comparison between experimental and simulated results,

$$T_{norm} = \frac{T - T_{min}}{T_{max} - T_{min}}, \quad (1)$$

where  $T_{max}$  denotes the maximum temperature within the region of interest during the modulation period, and  $T_{min}$  is the minimum temperature. In this case,  $T_{norm}$  becomes a function of thermal diffusivity and phase offset, which are the two variables to fit from the simulated temperature maps, but is independent of the heating power.

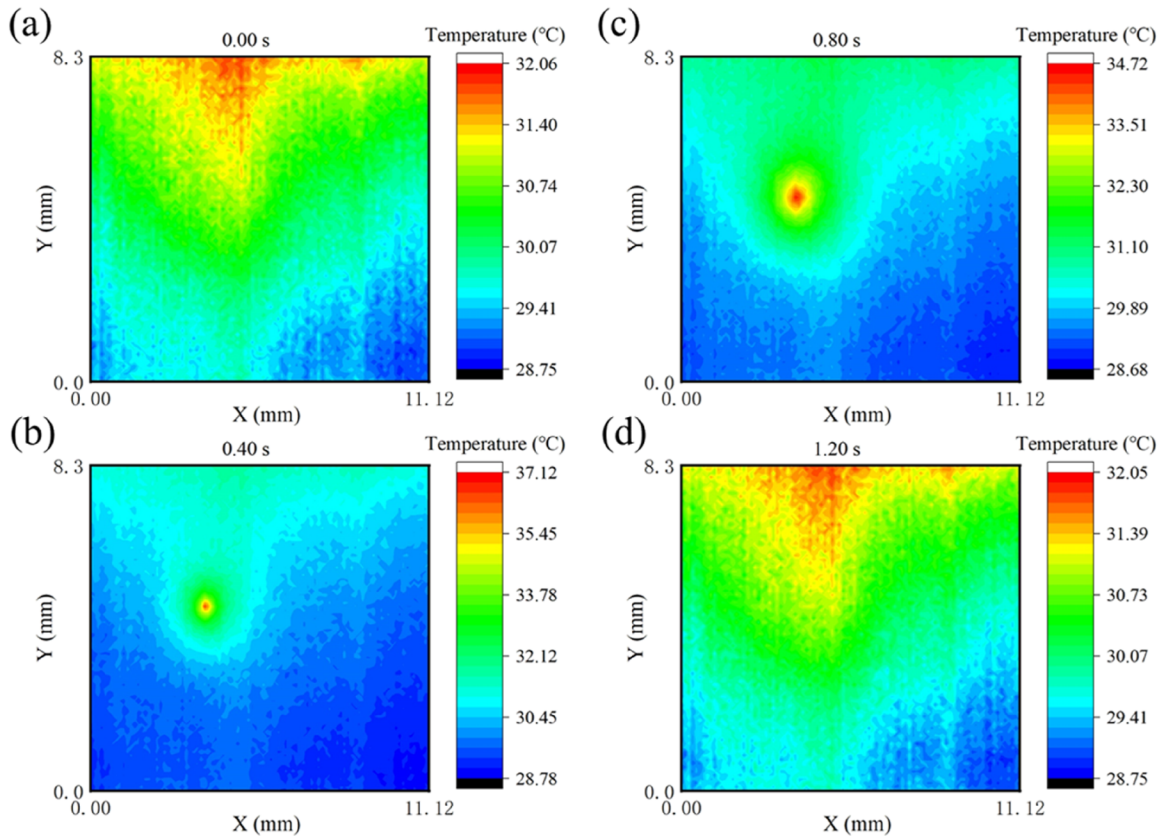


**FIG. 3.** Representative thermal images averaged at different times within one modulation period: (a) 0 s, (b) 0.4 s, (c) 0.8 s, and (d) 1.2 s. Note that the temperature scale bar varies with time to accommodate dynamic temperature changes.

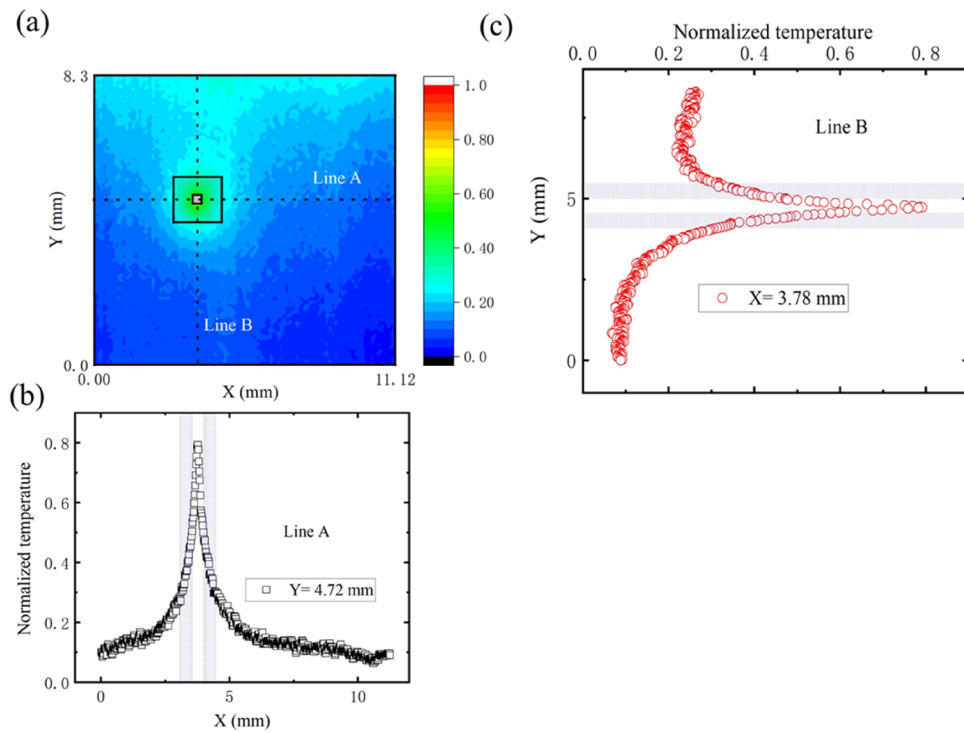


**FIG. 4.** Spatial distribution of normalized temperature recorded at 0.4 s. (a) Normalized thermogram corresponds to the thermogram shown in Fig. 3(b). [(b) and (c)] Normalized temperature along dashed Line A and Line B, respectively, both passing through the laser spot. The fitting was conducted using the temperature distribution within the dotted region centered on the laser spot.

Figure 4(a) shows a typical contour profile of  $T_{\text{norm}}$ , corresponding to the thermogram recorded at 0.4 s. Since the peak temperature during the modulation period occurs at 0.75 s,  $T_{\text{norm}}$  in the 0.4 s thermogram remains below 1. Figures 4(b) and 4(c) present the temperature distribution along Line A and Line B as indicated in Fig. 4(a). Due to measurement uncertainties, an abnormal temperature distribution is observed along Line B when the distance from the laser spot in the  $y$ -direction exceeds 0.80 mm. To evaluate the heat diffusion behavior, fitting is conducted using the temperature distribution within a square region centered on the laser spot, specifically spanning from -0.8 to 0.8 mm, as highlighted by the dotted region in Fig. 4(a). To minimize the influence of localized inhomogeneous heating at the laser focal point, data within the central region (-0.2–0.2 mm) were excluded from the fitting. Near the heating spot, both amplitude and phase lag were found to deviate from predictions of the heat conduction equations, a phenomenon also reported in previous lock-in thermography studies.<sup>6,11,12</sup> This deviation results in a pattern resembling an iris. Analogous to pupil exclusion in iris recognition to improve accuracy,<sup>21</sup> the central region around the laser focal point was omitted here to enhance the reliability of the fitting results.

### C. Numerical methods

The length ( $L$ ) and width ( $W$ ) of the test film should be significantly larger than the in-plane thermal diffusion length  $\delta_{\parallel}$ , defined as

$$\delta_{\parallel} = \sqrt{\frac{\alpha_{\parallel}}{\pi f_0}}, \quad (2)$$

where  $\alpha_{\parallel}$  is the in-plane thermal diffusivity. For stainless steel, with  $\alpha_{\parallel} = 3.6 \times 10^{-6} \text{ m}^2/\text{s}$ <sup>22</sup> and a modulation frequency  $f_0 = 0.8 \text{ Hz}$ , the calculated  $\delta_{\parallel}$  is  $\sim 1.5 \text{ mm}$ . Therefore, the film dimensions were set to  $L = W = 20 \text{ mm}$ , ensuring negligible edge effects.

Numerical simulations were conducted using the commercial CFD code Ansys FLUENT 19.0. The computational domain and boundary conditions are depicted in Fig. 5. All side surfaces were maintained at an isothermal condition of  $27^\circ\text{C}$ , the top surface is adiabatic, and the bottom surface was subjected to periodic laser heating. The heat flux follows the expression

$$q = \begin{cases} \frac{P}{\pi r_0^2} \exp\left(-\frac{x^2 + y^2}{r_0^2}\right), & 0 < \text{mod}\left(t - \frac{\phi}{2\pi f_0}, t_p\right) < t_p/2, \\ 0, & \text{otherwise,} \end{cases} \quad (3)$$

where  $P$  is the heating power,  $r_0$  is the beam radius, which is defined as the position where intensity falls to  $1/e^2$  of its maximum,  $t_p = 1/f_0$  is the modulation period, and  $\phi$  is the phase offset.

The computation domain is discretized using structured grids, as shown in Fig. 5. Considering the spatial resolution of the IR camera ( $20.0 \mu\text{m}/\text{pixel}$ ), to facilitate subsequent regression calculations, the grid size in both length and width directions was set to twice the spatial resolution ( $40 \mu\text{m}$ ). The total number of grid cells exceeded  $0.5 \times 10^6$ , providing sufficient resolution for capturing detailed temperature profiles.

Taking a  $20 \mu\text{m}$ -thick stainless-steel film as an example, with  $\alpha_{\parallel} = 3.6 \times 10^{-6} \text{ m}^2/\text{s}$  and  $\phi = 0$ , Fig. 5(b) shows a representative temperature contour recorded at 11.80 s. The temporal evolution of the normalized temperature  $T_{\text{norm}}$  at the location  $(-0.2 \text{ mm}, 0 \text{ mm})$  is

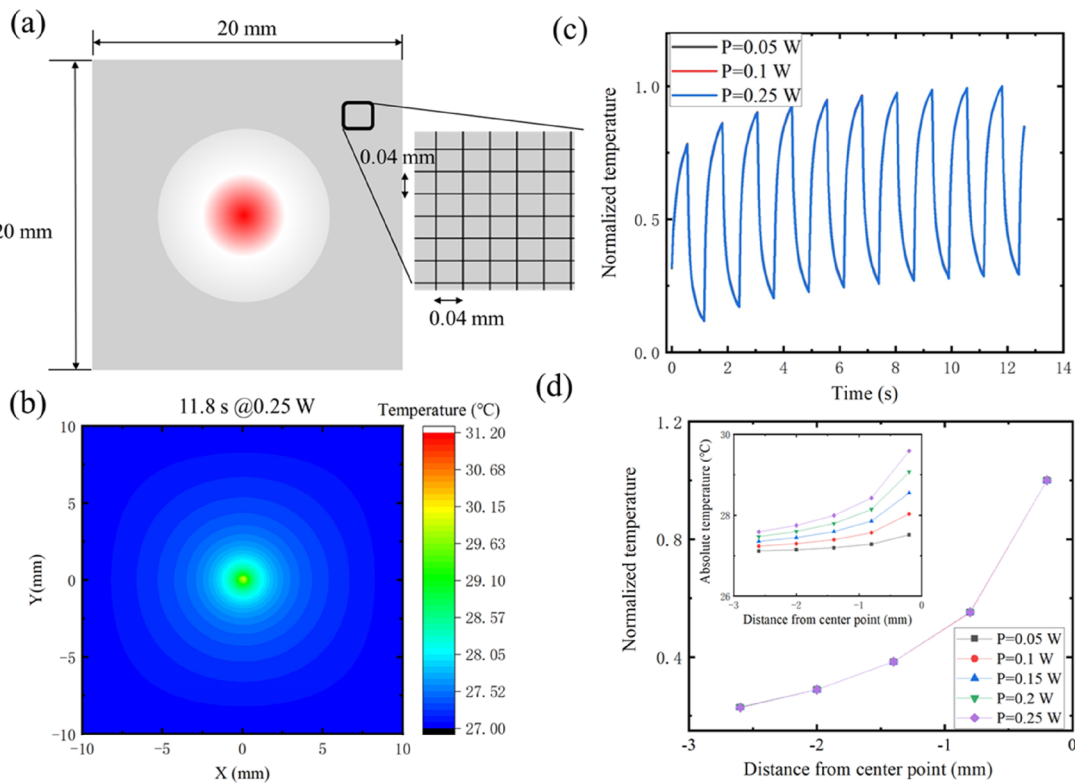


**FIG. 5.** Simulated transient thermal analysis of a periodically heated stainless-steel film with phase offset  $\phi = 0$ . (a) Schematic of the computational domain, with an enlarged view showing the structure mesh grid. (b) Simulated thermogram at 11.8 s under a heating power  $P = 0.25$  W. (c) Temporal evolution of normalized temperature  $T_{\text{norm}}$  at a representative location ( $-0.2$  mm,  $0$  mm), demonstrating convergence to a quasi-steady state after eight cycles. (d) Spatial distribution of  $T_{\text{norm}}$  at different heating powers.

09 August 2025 06:51:51

presented in Fig. 5(c). It is observed that the temperature reaches a quasi-steady periodic state after the ninth modulation cycle. In addition, Fig. 5(d) verifies that the spatial distribution of  $T_{\text{norm}}$  is also independent of the heating power.

#### D. Regression scheme

The regression problem is formulated as minimizing the Mean Absolute Error (MAE) between the measured and simulated temperatures within the masked square region centered on the laser spot, which can be written as

$$\begin{cases} \min MAE = \frac{1}{MN} \sum_{j=1}^M \sum_{i=1}^N |T_{\text{norm},i,j}^{\text{sim}} - T_{\text{norm},i,j}^{\text{exp}}|, \\ \alpha^{lower} \leq \alpha \leq \alpha^{upper}, \\ \phi^{lower} \leq \phi \leq \phi^{upper}. \end{cases} \quad (4)$$

Here,  $M$  is the number of time steps and  $N$  is the number of grids within the masked square region in Fig. 4(a). Superscripts upper and lower refer to the upper and lower bounds of the variables involved in the optimization.

The optimization procedure, as illustrated in Fig. 6, is based on the Bayesian optimization algorithm. A Gaussian Process model

serves as a surrogate to define both the prior distribution and likelihood distribution. The acquisition function, Expected Improvement, guides the selection of new sampling point  $x_{\text{new}}$  by quantifying the potentials for improvement over the current best solution. The entire intelligent optimization framework is implemented in Python through secondary development of ANSYS FLUENT, enabling integration of numerical simulation and regression analysis.<sup>23,24</sup>

The optimization process follows four key steps:

- (1) Generate an initial dataset  $X$ , where each point corresponds to a combination of the two variables,  $X_{\text{init}} = \{x = [\alpha_{\text{init}}, \phi_{\text{init}}]\}, x \in D^2$ .
- (2) Perform a Bayesian optimization to obtain the most promising evaluation point,  $x_{\text{new}}$ .
- (3) Output  $Loss$  through numerical calculation.
- (4) Update sample set  $X = X \cup (x_{\text{new}}, Loss_{\text{new}})$ , and repeat steps 2–3 until the convergence is achieved and the optimal solution  $x^*$  is obtained.

#### III. RESULTS AND DISCUSSION

To validate the proposed regression methodology, we measured the in-plane thermal diffusivity of a stainless-steel film with a thickness of  $20 \mu\text{m}$ . Both surfaces of the sample were coated with

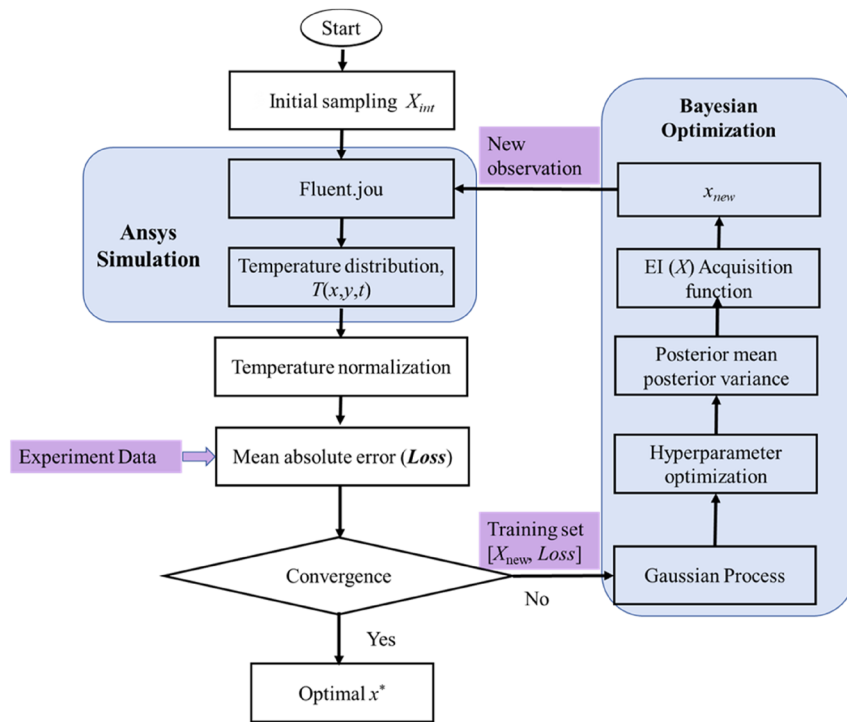


**FIG. 6.** Automated regression framework based on a Bayesian optimization algorithm. The algorithm is implemented in Python.

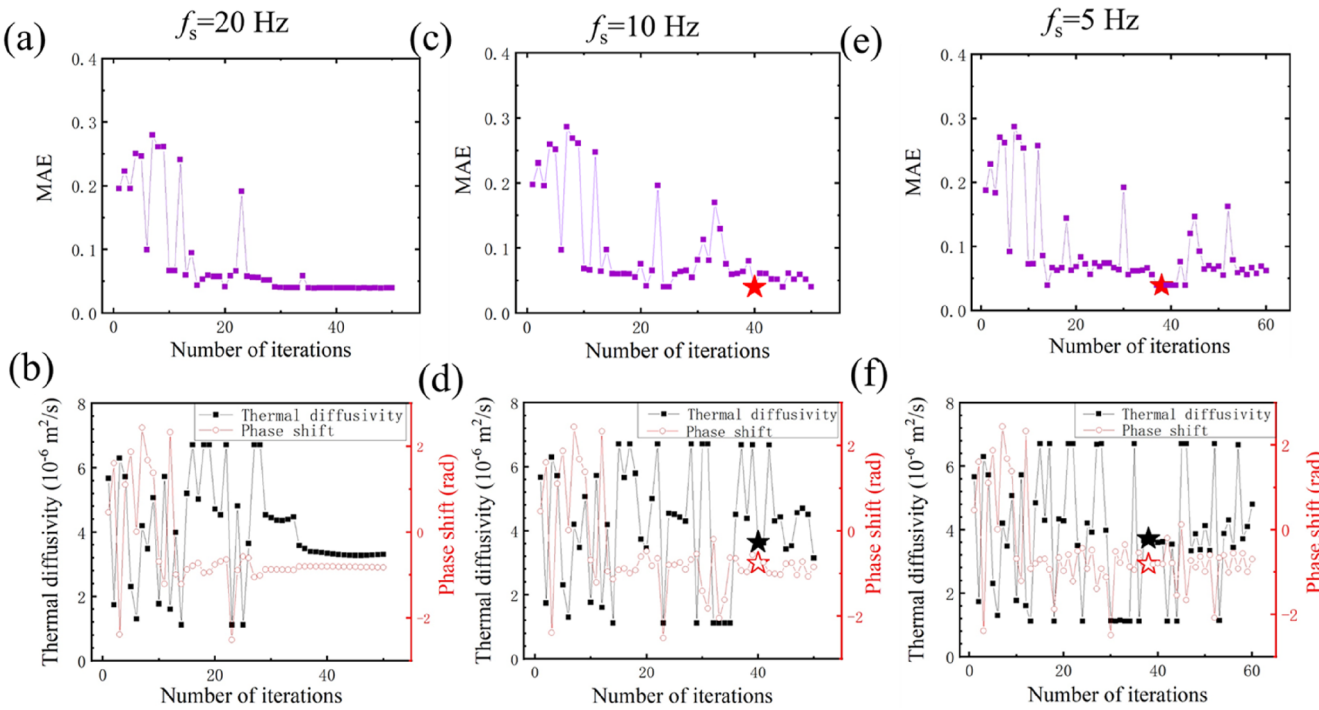


**FIG. 7.** Convergent trends under different sampling rates. The MAE, in-plane thermal diffusivity, and phase lag are plotted as functions of iteration number for sampling rates of [(a) and (b)] 20 Hz, [(c) and (d)] 10 Hz, and [(e) and (f)] 5 Hz. The optimal solution in each case is marked as a star.

graphite to ensure uniform laser absorption and infrared emission. The laser power was adjusted to maintain the maximum temperature rise below 10 °C, as shown in Fig. 3. The modulation frequency of the laser was 0.8 Hz, and thermograms were recorded at a sampling frequency of 20 Hz. The regression analysis was performed using normalized temperature data extracted from the square region centered on the laser spot, spanning from -0.8 to 0.8 mm in both lateral directions. To avoid localized non-uniform heating effects near the laser spot, the central region (-0.2–0.2 mm) was excluded. As a result, the total number of the spatial grids was  $N = 1500$ , and the number of temporal samples per modulation cycle was  $M = 25$ , yielding a total of 37 500 data for regression.

The initial sample set  $X$  in Fig. 6 consists of 12 randomly selected design points. To track the regression progress, the evolution of the MAE with iteration number is plotted in Fig. 7(a), while

the corresponding evaluated points  $x_{\text{new}} = [\alpha_{\text{new}}, \phi_{\text{new}}]$ , obtained from the surrogate model in each iteration, are shown in Fig. 7(b). The MAE stabilizes after ~35 iterations. The thermal diffusivity is determined to be  $3.34 \pm 0.06 \times 10^{-6} \text{ m}^2/\text{s}$ , in good agreement with reference values obtained in vacuum using a micro-thermocouple.<sup>22</sup> For comparison, conventional lock-in thermography conducted at a sampling frequency of 25 Hz typically requires a modulation frequency as low as 0.1 Hz to ensure phase accuracy.<sup>6</sup> To eliminate the influence of convective heat loss, the product of the two slopes, i.e., the slope  $k_\phi$  of phase lag  $\phi$  vs distance  $r$ , and the slope  $k_T$  of  $\ln(|T| \times r^{0.5})$  vs  $r$  is commonly used to determine the in-plane thermal diffusivity,

$$\alpha_{//} = \frac{\pi f_0}{k_\phi \times k_T}. \quad (5)$$

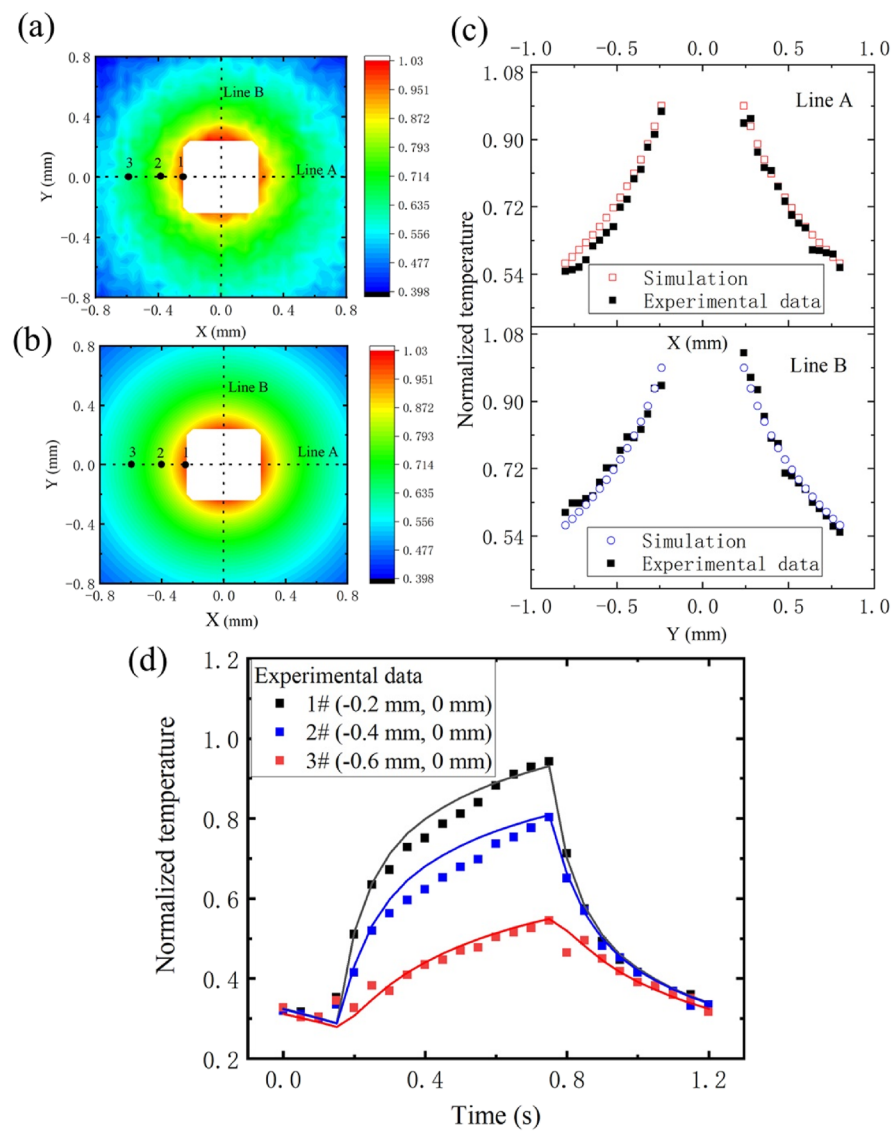


**FIG. 8.** Comparison of experimental and simulated results using the optimal solution  $x^* = [\alpha^* = 3.34 \times 10^{-6} \text{ m}^2/\text{s}, \phi^* = -0.808 \text{ rad}]$ . (a) Experimental and (b) simulated normalized temperature distribution in the fitting region, with the central white square denoting the excluded area near the laser spot. (c) Normalized temperature profiles along dashed Line A and Line B indicated in [(a) and (b)]. (d) Temporal evolution of normalized temperature at three representative locations.

It is worth noting that this regression methodology inherently incorporates information from both the temperature amplitude and phase, thereby eliminating the need to explicitly account for convective heat loss in the simulation.

Using the optimal solutions,  $\alpha_{//} = 3.34 \times 10^{-6} \text{ m}^2/\text{s}$  and  $\phi = -0.808 \text{ rad}$ , good agreement is observed between the normalized temperature  $T_{\text{norm}}$  contours obtained from experimental data [Fig. 8(a)] and simulation results [Fig. 8(b)]. Two representative curves across the laser spot are compared in Fig. 8(c). Despite scattering in the experimental data due to measurement uncertainties, the values within the fitting region show close alignment with the simulation. Figure 8(d) shows the temporal evolution of  $T_{\text{norm}}$  at three representative locations. Point 1# ( $-0.2 \text{ mm}, 0 \text{ mm}$ ) lies on the inner boundary of the fitting region, and  $T_{\text{norm}}$  approaches unit at  $0.75 \text{ s}$ , consistent with the expected peak temperature. Based on the linear dependence between  $\phi$  and distance  $r$ ,<sup>4,6</sup> a change in  $r$  from  $0.2$  to  $0.6 \text{ mm}$  should result in a phase shift of  $\sim 0.3 \text{ rad}$ . However, this variation is difficult to resolve in Fig. 8(d), suggesting that the proposed regression method is weakly sensitive to measurement noise in the phase lag. This robustness enables its application in a range of scenarios, such as characterizing the thermal properties of inhomogeneous composite films with spatially varying structures. For such materials, conventional lock-in thermography, which relies on linear fitting of  $\phi$  vs  $r$ , can introduce significant errors. In contrast, the proposed regression methodology leverages both spatial and temporal temperature data to extract an effective thermal diffusivity, providing improved accuracy and reliability.

To evaluate the influence of sampling rate on the regression process, we down-sampled the experimental thermograms. At a modulation frequency of  $f_0 = 0.8 \text{ Hz}$  and a frame rate of  $20 \text{ Hz}$ ,  $25$  frames per modulation period were fed into the regression. Reducing this by half yields a  $10 \text{ Hz}$  sampling rate and  $13$  frames per modulation period. The convergence behavior at  $10 \text{ Hz}$  is shown in Figs. 7(c) and 7(d). Compared to the  $20 \text{ Hz}$  case, the MAE exhibits more fluctuation after the 35th iteration, indicating that the convergence deteriorates as the frame rate decreases. While the estimated  $\phi$  remains relatively stable, the inferred  $\alpha_{//}$  varies significantly. This behavior indicates that the thermograms are phase-sensitive. Small phase changes lead to large variations in MAE and consequently in the calculated thermal diffusivity. Nevertheless, the optimal solution identified at  $10 \text{ Hz}$  is  $\alpha^* = 3.65 \times 10^{-6} \text{ m}^2/\text{s}$  and  $\phi = -0.758 \text{ rad}$ , which remains within the acceptable error margin. Similar trends are observed at a sampling rate of  $5 \text{ Hz}$ , where only seven frames are used per modulation period. The optimal solution in this case is  $\alpha^* = 3.72 \times 10^{-6} \text{ m}^2/\text{s}$  and  $\phi = -0.807 \text{ rad}$ . Notably, the ability to extract accurate thermal properties with such low sampling rates significantly relaxes the performance requirements for the IR detector, enhancing the practicality of the method.

#### IV. CONCLUSIONS

We proposed a robust regression methodology for determining the in-plane thermal diffusivity of thin films using IR thermography. Time-sequential thermograms, recorded with a free-running, non-research-grade IR camera, were directly integrated into the regression process. The thermal diffusivity and phase offset were

automatically extracted by minimizing the MAE between measured and simulated normalized temperatures within a Bayesian optimization framework. Validation on a stainless-steel film yielded a thermal diffusivity of  $3.34 \times 10^{-6} \text{ m}^2/\text{s}$ . Convergence analyses at different sampling rates demonstrated the method's robustness and practical feasibility, even under reduced frame rates. Compared to conventional lock-in thermography, the proposed framework significantly reduces system requirements, making it particularly promising for characterizing composite films and advanced thermal interfacial materials.

#### ACKNOWLEDGMENTS

The authors gratefully acknowledge the support provided by the National Natural Science Foundation of China (Grant No. 52376159).

#### AUTHOR DECLARATIONS

##### Conflict of Interest

The authors have no conflicts to disclose.

##### Author Contributions

**Maochao Lv:** Conceptualization (equal); Data curation (equal); Formal analysis (equal); Investigation (equal); Methodology (equal); Validation (equal); Visualization (equal); Writing – original draft (equal); Writing – review & editing (equal). **Qinmeng Jiang:** Data curation (equal); Investigation (equal); Methodology (equal); Software (equal); Validation (equal); Visualization (equal); Writing – review & editing (equal). **Hui Liu:** Supervision (equal); Writing – review & editing (equal). **Yanhui Zhang:** Data curation (equal); Formal analysis (equal); Investigation (equal); Writing – review & editing (equal). **Jie Yang:** Data curation (equal); Formal analysis (equal); Investigation (equal); Writing – review & editing (equal). **Jianli Wang:** Conceptualization (equal); Funding acquisition (equal); Methodology (equal); Supervision (equal); Writing – review & editing (equal).

#### DATA AVAILABILITY

The data that support the findings of this study are available from the corresponding authors upon reasonable request.

#### REFERENCES

- <sup>1</sup>C.-P. Feng, L.-Y. Yang, J. Yang, L. Bai, R.-Y. Bao, Z.-Y. Liu, M.-B. Yang, H.-B. Lan, and W. Yang, *Compos. Commun.* **22**, 100528 (2020).
- <sup>2</sup>P. Zhang, X. Ming, Y. Liu, X. Wang, H. Shi, Y. Hao, J. Lu, Z. Liu, H. Lai, Y. Zhang, W. Gao, Z. Xu, and C. Gao, *J. Therm. Sci.* **33**, 1480 (2024).
- <sup>3</sup>A. Wolf, P. Pohl, and R. Brendel, *J. Appl. Phys.* **96**, 6306 (2004).
- <sup>4</sup>A. Mendioroz, R. Fuente-Dacal, E. Apíñaniz, and A. Salazar, *Rev. Sci. Instrum.* **80**, 074904 (2009).
- <sup>5</sup>P. W. Nolte, T. Malvisalo, F. Wagner, and S. Schweizer, *Quant. InfraRed Thermogr. J.* **14**, 218 (2017).
- <sup>6</sup>T. Ishizaki and H. Nagano, *Infrared Phys. Technol.* **99**, 248 (2019).

- <sup>7</sup>K. Miyachi, Y. Muranaka, S. Nonaka, A. Ueno, and H. Nagano, *Infrared Phys. Technol.* **115**, 103743 (2021).
- <sup>8</sup>A. Bedoya, F. Rodríguez-Valdés, and E. Marín, *Infrared Phys. Technol.* **137**, 105161 (2024).
- <sup>9</sup>A. Bedoya, A. Salazar, A. Mendioroz, and E. Marín, *J. Appl. Phys.* **135**, 135102 (2024).
- <sup>10</sup>A. Salazar and A. Mendioroz, *Int. J. Therm. Sci.* **214**, 109928 (2025).
- <sup>11</sup>D. Wang, H. Ban, and P. Jiang, *Int. J. Heat Mass Transfer* **242**, 126886 (2025).
- <sup>12</sup>M. Lv, J. Yang, Y. Zhang, J. Wang, and Y. Zhou, *Int. J. Thermophys.* **46**, 17 (2025).
- <sup>13</sup>S. Kaipalavil and A. Mandelis, *Nat. Photonics* **8**, 635 (2014).
- <sup>14</sup>Z. Luo, H. Luo, S. Wang, F. Chen, Z. Su, P. Shen, and H. Zhang, *IEEE Trans. Ind. Inf.* **18**, 8641 (2022).
- <sup>15</sup>S. Schmid, J. Reinhardt, and C. U. Grossé, *NDT E Int.* **143**, 103063 (2024).
- <sup>16</sup>T. Ishizaki, T. Igami, and H. Nagano, *Rev. Sci. Instrum.* **91**, 064901 (2020).
- <sup>17</sup>J. Liu, W. Yang, and J. Dai, *Infrared Phys. Technol.* **53**, 348 (2010).
- <sup>18</sup>O. Breitenstein, W. Warta, and M. Langenkamp, *Lock-in Thermography: Basics and Use for Evaluating Electronic Devices and Materials* (Springer, Berlin, Heidelberg, Germany, 2010).
- <sup>19</sup>B. A. F. Kopera and M. Retsch, *Rev. Sci. Instrum.* **92**, 014902 (2021).
- <sup>20</sup>R. Smith, in *Ninth International Conference on Document Analysis and Recognition (ICDAR 2007)* (IEEE, 2007), p. 629.
- <sup>21</sup>V. Panwar and Pooja, in *2022 International Conference on Computing, Communication, and Intelligent Systems (ICCCIS)* (IEEE, 2022), p. 857.
- <sup>22</sup>Y. Zhang, R. Xu, Y. Liu, Q. Jiang, Q. Li, Y. Liu, and J. Wang, *Int. J. Heat Mass Transfer* **227**, 125536 (2024).
- <sup>23</sup>Y. Chen, H. Chen, H. Zeng, J. Zhu, K. Chen, Z. Cui, and J. Wang, *Appl. Therm. Eng.* **213**, 118755 (2022).
- <sup>24</sup>Q. Jiang, Y. Zhang, Y. Liu, R. Xu, J. Zhu, and J. Wang, *J. Energy Storage* **91**, 112136 (2024).